THE JOURNAL OF BIOLOGICAL CHEMISTRY VOL. 289, NO. 40, pp. 27836–27848, October 3, 2014

Kinesin-2 KIF3AB Exhibits Novel ATPase Characteristics*[S]

Received for publication, May 24, 2014, and in revised form, August 8, 2014 Published, JBC Papers in Press, August 13, 2014, DOI 10.1074/jbc.M114.583914

Clayton D. Albracht[‡1], **Katherine C. Rank**[§1,2], **Steven Obrzut**[‡], **Ivan Rayment**[§3], **and Susan P. Gilbert**[‡4]

From the [‡]*Department of Biological Sciences and the Center for Biotechnology and Interdisciplinary Studies, Rensselaer Polytechnic Institute, Troy, New York 12180 and the* [§]*Department of Biochemistry, University of Wisconsin, Madison, Wisconsin 53706*

Background: KIF3AB is a heterotrimeric plus-end-directed kinesin-2 motor, implicated in intraflagellar transport.
Results: KIF3AB shows rate-limiting ADP release upon microtubule collision and an unusual apparent weak ATP affinity observed at microtubule·KIF3AB dissociation.
Conclusion: The presteady-state kinetics suggest a novel ATPase mechanism for KIF3AB stepping.
Significance: The KIF3AB kinetics reveal the mechanistic diversity that kinesin motors exhibit for cargo transport.

KIF3AB is an N-terminal processive kinesin-2 family member best known for its role in intraflagellar transport. There has been significant interest in KIF3AB in defining the key principles that underlie the processivity of KIF3AB in comparison with homodimeric processive kinesins. To define the ATPase mechanism and coordination of KIF3A and KIF3B stepping, a presteady-state kinetic analysis was pursued. For these studies, a truncated murine KIF3AB was generated. The results presented show that microtubule association was fast at 5.7 μM^{-1} s^{-1}, followed by rate-limiting ADP release at 12.8 s^{-1}. ATP binding at 7.5 μM^{-1} s^{-1} was followed by an ATP-promoted isomerization at 84 s^{-1} to form the intermediate poised for ATP hydrolysis, which then occurred at 33 s^{-1}. ATP hydrolysis was required for dissociation of the microtubule·KIF3AB complex, which was observed at 22 s^{-1}. The dissociation step showed an apparent affinity for ATP that was very weak ($K_{½,ATP}$ at 133 μM). Moreover, the linear fit of the initial ATP concentration dependence of the dissociation kinetics revealed an apparent second-order rate constant at 0.09 μM^{-1} s^{-1}, which is inconsistent with fast ATP binding at 7.5 μM^{-1} s^{-1} and a $K_{d,ATP}$ at 6.1 μM. These results suggest that ATP binding *per se* cannot account for the apparent weak $K_{½,ATP}$ at 133 μM. The steady-state ATPase $K_{m,ATP}$, as well as the dissociation kinetics, reveal an unusual property of KIF3AB that is not yet well understood and also suggests that the mechanochemistry of KIF3AB is tuned somewhat differently from homodimeric processive kinesins.

The kinesin-2 subfamily includes microtubule-based molecular motors made up of heterotrimeric and homodimeric molecular motors. One family member, KIF3, has been identified across organisms from *Chlamydomonas* to humans and, in higher eukaryotes, consists of two non-identical N-terminal motor polypeptides that bind to a non-motor kinesin-associated protein KAP at the C-terminal cargo domains forming the functional heterotrimer (1–12). In mammals, KIF3A binds either to KIF3B or KIF3C to form the heterodimeric motor that binds to KAP. KIF3AC is better known for transport roles in neuronal tissues as well as microtubule cytoskeleton remodeling (13, 14).

KIF3AB is best known as the core intraflagellar transport protein responsible for anterograde transport that works in concert with cytoplasmic dynein as the essential motor proteins for assembly and maintenance of cilia and flagella (11, 12, 15–18). A deletion of KIF3A leads to the mislocalization of opsin and arrestin in the highly organized cilia of photoreceptor cells (18). Additionally, KIF3AB has been implicated in the transport of fodrin-associated vesicles along neuronal axons (19) and is required for the production of cilia that are crucial for the proper mesodermal patterning during neurogenesis to establish the left-right body asymmetry (20–22) In addition, KIF3AB has well documented roles in pigment granule transport (5, 23). To better understand the complex intramolecular and intermolecular communication required for these highly ordered and distinctive transport and signaling pathways, it is necessary to define the biophysical properties that regulate this motor.

Heterotrimeric kinesin-2 has been of interest since 1992 (24); however, detailed studies of its mechanochemistry have yet to be performed. Progress in studying the biochemical pathway has been hindered by a lack of sufficient materials. Instead, experiments have focused on KIF3AB homologs in various model organisms and single molecule studies of these homologs to better understand the kinesin-2 family members. Single molecule studies using full-length *M. musculus* KIF3AB measured the mean velocity at 436 nm/s (25). Chimeric motors using the kinesin-1 kinesin heavy chain rod domain with chimeric *M. musculus* KIF3AA motor heads demonstrated that processivity scaled inversely with increased neck linker length (26). In contrast, single molecule studies using the *Caenorhabditis elegans* KIF3AB homolog, KLP20/KLP11, found homodimeric KLP11 (KIF3B) to be unprocessive, yet heterodimeric KLP20/KLP11 was processive (27). These results showed that heterodimerization was required for processivity and clearly

* This work was supported, in whole or in part, by National Institutes of Health Grants R37-GM54141 (to S. P. G) and R01-GM086351 (to I. R.).
[S] This article contains supplemental Video 1.
[1] Both authors contributed equally to this work.
[2] Supported by National Institutes of Health Training Grant T32-GM07215.
[3] To whom correspondence may be addressed: Dept. of Biochemistry, University of Wisconsin, Madison, WI 53706. Tel.: 608-262-0437; E-mail: ivan_rayment@biochem.wisc.edu.
[4] To whom correspondence may be addressed: Dept. of Biological Sciences, Rensselaer Polytechnic Institute, 110 8th St., Troy, NY 12180. Tel.: 518-276-4415; E-mail: sgilbert@rpi.edu.

documented the influence of KLP20 on KLP11. Single molecule studies of the *Xenopus laevis* KIF3AB homolog XkplA/B revealed that kinesin-2 generates force similar to conventional kinesin-1, yet kinesin-2 XkplA/B was more likely to detach from the microtubule at this stall force than kinesin-1 (28). In addition, studies using suspended microtubules to measure the torque of the *M. musculus* KIF3AB upon microtubules found no signs of torque generation, leading to the conclusion that the processive run is along a single protofilament (29). Although these studies have provided a better understanding of the single molecule characteristics, there remain questions about properties that are species-specific as compared with conserved attributes of the KIF3AB homologs. Additionally, there has not been a comprehensive analysis of the ATPase cycle reported that focuses on understanding the coupling of the ATP turnover to processive stepping.

KIF3AB provides a unique and challenging model to define the mechanochemical properties of a kinesin-2 because the polypeptides and the motor heads of KIF3A and KIF3B are not identical, and each may have distinctive properties that contribute to transport roles of the heterodimeric motor. In this study, an *M. musculus* KIF3AB heterodimer was used that includes the respective native motor domains, neck region, and three native heptads of coiled-coil prior to a synthetic heterodimerization domain (SHD)[5] that stabilizes the KIF3AB heterodimeric state. This strategy resulted in the ability to purify milligram quantities of well behaved KIF3AB motors from a bacterial expression system that made the presteady-state kinetic analysis possible. The experimental results show that ADP release upon MT collision is rate-limiting and that there is an apparent weak affinity for ATP at the MT·KIF3AB dissociation step that was also detected in the steady-state ATPase kinetics. These unique characteristics were not observed previously for the well characterized homodimeric kinesins, conventional kinesin-1 KHC, kinesin-5 (Eg5), or kinesin-7 (CENP-E). Therefore, these studies on KIF3AB provide key insights into the fundamental characteristics that evolved to give kinesin-2s their unique physiological roles in organelle trafficking and signal transduction.

EXPERIMENTAL PROCEDURES

Construct Design—M. musculus KIF3A and *KIF3B* genes were the generous gift of William O. Hancock (Pennsylvania State University), and each gene was modified using the QuikChange mutagenesis protocol as described previously (30). The spurious mutations subsequently identified in the original materials were rectified to match the published sequences (31). The generated constructs were sequence-verified over the entire ORF insert. Fig. 1 shows the engineered KIF3AB heterodimer used in this study, in which stable dimerization was achieved through inclusion of an SHD motif containing either an acidic or a basic helix (32, 33). The KIF3A-AHD polypeptide consisted of the motor domain, neck linker, and three heptads of native helix sequence followed by the acidic synthetic fusion helix (AHD). The *KIF3A-AHD* construct was amplified and introduced into a modified pET31b plasmid (Novagen) that contains the C-terminal AHD fusion sequence, a TEV protease site, and a StrepII tag. The KIF3B-BHD polypeptide contained the motor domain, neck linker, and three heptads of native helix sequence followed by the basic fusion helix (BHD), a TEV protease site, and then finally a His_8 tag. The *KIF3B-BHD* gene was amplified and introduced into a modified pET24d (Novagen) plasmid containing the C-terminal BHD fusion followed by a TEV protease site and His_8 tag. The expressed sequences of *KIF3A-AHD* and *KIF3B-BHD* are as follows, where the amino acid residues in boldface type denote the SHD fusion sequence: KIF3A(Met^1–Glu^{376})-**LEKEIAALEKEIAALEK**TTSENLYFQGASNWSHPQFEK (predicted molecular weight = 46,341); KIF3B(Met^1–Lys^{371}), **LKEKIAALKEKIAALKE**TTSENLYFQGASHHHHHHHH (predicted molecular weight = 45,790).

Protein Expression and Purification—KIF3A-AHD and *KIF3B-BHD* plasmids (100 ng each) were co-transformed into chemically competent *Escherichia coli* BL21-CodonPlus (DE3)-RIL cells (Stratagene, Inc.) and applied to selective LB plates containing 100 μg/ml ampicillin, 50 μg/ml kanamycin, and 10 μg/ml chloramphenicol. Positive colonies were selected and grown in liquid LB with antibiotics at 37 °C until A_{600} was ~0.5 and then cooled on ice to shift the temperature to 16 °C. Protein expression was induced with 0.2 mM isopropyl 1-thio-β-D-galactopyranoside, shaking at 185 rpm at 16 °C for ~15 h. The cell pellets were collected by centrifugation and subsequently resuspended (1 g/10 ml of buffer) and lysed in 10 mM sodium phosphate buffer, pH 7.2, 300 mM NaCl, 2 mM $MgCl_2$, 0.1 mM EGTA, 10 mM PMSF, 1 mM DTT, 0.2 mM ATP, and 30 mM imidazole containing 0.1 mg/ml lysozyme for 30 min at 4 °C with gentle stirring. Following three cycles of freezing (liquid N_2) and thawing (37 °C), the cell lysate was clarified by ultracentrifugation, and the soluble cell extract was loaded onto a HisTrap FF Ni^{2+}-NTA column (GE Healthcare) that was pre-equilibrated in Ni^{+2}-NTA binding buffer: 20 mM sodium phosphate buffer, pH 7.2, 300 mM NaCl, 2 mM $MgCl_2$, 0.1 mM EGTA, 0.2 mM ATP, and 30 mM imidazole. The column was washed with Ni^{+2}-NTA binding buffer, and KIF3AB was eluted in 2-ml fractions using the Ni^{+2}-NTA binding buffer at 200 mM imidazole. Fractions containing KIF3AB were identified by SDS-PAGE and then loaded onto a pre-equilibrated StrepTactin™ column (StrepTrapII HP, GE Healthcare) at 20 mM sodium phosphate buffer, pH 7.2, 300 mM NaCl, 2 mM $MgCl_2$, 0.1 mM EGTA, 0.2 mM ATP. After washing the StrepTrap column to return the absorbance to baseline, KIF3AB was eluted as 2-ml fractions with the StrepTrap binding buffer plus 2.5 mM desthiobiotin. Fractions enriched in KIF3AB were pooled, concentrated by ultrafiltration, and dialyzed overnight in 20 mM HEPES, pH 7.2, with KOH, 0.1 mM EDTA, 5 mM magnesium acetate, 50 mM potassium acetate, 1 mM DTT, 5% sucrose, 100 mM NaCl. The dialyzed protein was clarified by ultracentrifugation, and KIF3AB heterodimerization state was confirmed by analytical gel filtration (Fig. 2*A*) and SDS-PAGE (Fig. 2*A*, *inset*). Aliquots of KIF3AB were frozen in liquid N_2 and stored at −80 °C.

[5] The abbreviations used are: SHD, synthetic heterodimer domain; MT, microtubule; AHD, acidic heterodimerization domain; BHD, basic heterodimerization domain; AMPPNP, adenosine 5′-(β,γ-imido)triphosphate; ATPγS, adenosine-5′-(γ-thio)-triphosphate; mant, 2′-(or 3′)-*O*-(*N*-methylanthraniloyl); TEV, tobacco etch virus; NTA, nitrilotriacetic acid; KHC, kinesin-1 heavy chain.

Analytical Gel Filtration Chromatography—KIF3AB was clarified (90,000 rpm for 10 min at 4 °C, Beckman Coulter TLA 100 rotor, Beckman Coulter Optima TLX Ultracentrifuge), and the protein concentration was determined by the Bio-Rad protein assay using IgG as a protein standard. KIF3AB at 6, 12, and 25 μM (heterodimer concentration) or protein standards at 25 μM were loaded onto the HPLC gel filtration column (Superose^{TM} 10/300, GE Healthcare Life Sciences) with elution at 20 mM HEPES, pH 7.2, with KOH, 0.1 mM EDTA, 0.1 mM EGTA, 5 mM magnesium acetate, 50 mM potassium acetate, 1 mM DTT plus 100 mM NaCl using a Beckman Coulter System Gold HPLC. Protein elution was determined by intrinsic fluorescence detection (Jasco FP-2020, Victoria, British Columbia) as described previously (34, 35). Equation 1 was used to determine the partition coefficients of standards relative to KIF3AB, where V_e is the elution volume, V_t is the total volume, and V_0 is the void volume.

$$K_{av} = (V_e - V_0)/(V_t - V_0) \quad \text{(Eq. 1)}$$

The Stokes radii of each of the five standards are as follows: avidin, 2.3 nm; ovalbumin, 3.0 nm; bovine serum albumin (BSA), 3.5 nm; IgG, 3.9 nm; and catalase, 5.2 nm. The linear fit of the data for the plot of $(-\log K_{av})^{1/2}$ *versus* Stokes radius enabled the Stokes radius to be determined for KIF3AB (Fig. 2*B*).

The relative molecular mass (M_r) was calculated for KIF3AB as described previously (35). Fig. 2*C* shows the semilog plot of K_{av} *versus* $\log M_r$ using the known standards: BSA (67,000 Da), IgG (120,000 Da), and catalase (250,000 Da).

KIF3AB-promoted Microtubule Gliding—Microtubule gliding assays were used to characterize the motility of KIF3AB, as described previously (36). The PME-80 motility buffer (80 mM PIPES, pH 6.9, with KOH, 5 mM $MgCl_2$, and 1 mM EGTA) was supplemented with 1.5 mM magnesium acetate, 0.25 mg/ml casein, 25 mM glucose, 0.2 mg/ml glucose oxidase, 175 μg/ml catalase, 0.3 mg/ml creatine phosphokinase, 2 mM phosphocreatine, 15 μM paclitaxel, and 1 mM ATP. The microtubule movement was measured with time lapse image capture total internal reflection fluorescence microscopy using a Zeiss AxioObserver Z1 Inverted Laser TIRF3 microscope system with a Hamamatsu EM-CCD digital camera and a 561-nm laser for excitation. Time lapse sequences were taken for a 180-ms exposure time, with images taken every 20 s for 15 min and analyzed by tracking individual microtubules as they were propelled by the coverslip-attached motors as described previously (36). The direction and distance of gliding were quantified as a function of time using Zeiss AxioVision version 4.8.2 software to determine the velocity of motility that was promoted by KIF3AB (Fig. 2*D*). The criteria for analysis were that MTs must be 3–8 μm in length with movement occurring completely in the field of focus and without pauses. Approximately 15–20 MTs were quantified per video.

Before each experiment, KIF3AB was clarified (90,000 rpm for 10 min at 4 °C, Beckman Coulter TLA 100 rotor, Beckman Coulter Optima TLX Ultracentrifuge), and the protein concentration was determined by the Bio-Rad protein assay using IgG as a protein standard. For the experiments presented here, the purification tags were not removed, and the protein concentration is reported as the KIF3AB heterodimer (molecular weight = 92,131) with the ATP site concentration at two nucleotide sites per KIF3AB heterodimer.

Experimental Conditions—The experiments were performed at 25 °C in ATPase buffer: 20 mM HEPES, pH 7.2, with KOH, 0.1 mM EDTA, 0.1 mM EGTA, 5 mM magnesium acetate, 50 mM potassium acetate, 1 mM DTT, and 5% sucrose. The MT or tubulin polymer concentrations reported resulted from bovine tubulin that was cold-depolymerized, clarified, and polymerized with 1 mM MgGTP at 37 °C, followed by MT stabilization with 40 μM paclitaxel (37, 38). The reported concentrations of nucleotides (ATP and GTP) and nucleotide analogs (mantATP, mantADP, AMPPNP, and ATPγS) also include an equivalent concentration of magnesium acetate. The fluorescent analogs mantATP and mantADP were purchased from Invitrogen as the racemate mixture. Errors are reported as S.E.

KIF3AB Steady-state ATP Turnover—The steady-state ATPase was measured by following the hydrolysis of [α-^{32}P]ATP to [α-^{32}P]ADP·P_i as described previously (39). The Michaelis-Menten equation was fit to the observed rates of ATP turnover as a function of MgATP concentration (Fig. 3*A*) with the rate quantified from the concentration of ATP binding sites of the KIF3AB heterodimer. The enzyme concentration at 0.5 μM was not 10-fold less than the $K_{½MT}$, which required that quadratic Equation 2 be used to fit the MT concentration dependence (Fig. 3*B*).

$$\text{Rate} = 0.5 \times (k_{cat}/E_0)((E_0 + K_{1/2,MT} + MT_0) - ((E_0 + K_{1/2,MT} + MT_0)^2 - (4E_0MT_0))^{1/2}) \quad \text{(Eq. 2)}$$

Rate (s^{-1}) is expressed as μM ADP·P_i produced/s/ATP binding site, and k_{cat} is the maximum rate constant of steady-state ATP turnover. E_0 is the concentration of KIF3AB ATP binding sites in the experiment, $K_{½,MT}$ is the concentration of tubulin polymer that provides one-half the maximum rate of steady-state ATP turnover, and MT_0 is the tubulin polymer concentration.

Kinetics of KIF3AB MT Association and MantADP Release upon MT Collision—The ADP at the active sites of KIF3AB was exchanged with the fluorescent analog mantADP at a concentration of 5 μM KIF3AB nucleotide sites and 30 μM mantADP (1:6 ratio). Subsequently, the KIF3AB·mantADP complex was transferred to a KinTek SF2003 stopped-flow instrument (Kintek Corp., Austin, TX) and rapidly mixed with varying concentrations of MTs plus 2 mM MgATP (syringe concentration). The fluorescence change was monitored as a function of time (λ_{ex} = 360 nm, λ_{em} = 450 nm; detected using a 409-nm long pass filter). A double exponential function was used to fit the biphasic transients, and the observed rates of the initial fast exponential phase were plotted as a function of increasing MT concentrations.

$$k_{obs} = k_{+1}[\text{MTs}] + k_{-1} \quad \text{(Eq. 3)}$$

At low MT concentrations (0.5–1.5 μM), the rate of mantADP release is limited by MT collision; therefore, in this MT concentration range, the linear fit of the data provides the second-order rate constant for MT association, k_{+1}, with the KIF3AB

$$\mathrm{MT + E{\bullet}ADP \overset{1}{\rightleftarrows} MT{\bullet}E{\bullet}ADP \overset{2}{\rightleftarrows} MT{\bullet}E + ADP}$$

$$\mathrm{MT{\bullet}E + ATP \overset{3}{\rightleftarrows} MT{\bullet}E{\bullet}ATP \overset{3'}{\rightleftarrows} MT{\bullet}E^{*}{\bullet}ATP \overset{4}{\rightleftarrows} MT{\bullet}E{\bullet}ADP{\bullet}P_i \overset{5}{\rightleftarrows} MT + E{\bullet}ADP + P_i}$$

SCHEME 1

off rate, k_{-1}, as defined by the *y* intercept. At higher concentrations of MTs, mantADP release after MT collision becomes rate-limiting, and the hyperbolic fit of the data provides the maximum rate constant of mantADP release, k_{+2} (see Fig. 4, Scheme 1, and Table 1).

Kinetics of MantATP Binding—MT·KIF3AB complexes were preformed and rapidly mixed in the stopped-flow instrument with mantATP ($\lambda_{ex} = 360$ nm, $\lambda_{em} = 450$ nm; detected using a 409-nm long pass filter). The resulting transients were biphasic and revealed a fluorescence enhancement due to mantATP entering the hydrophobic environment of the active site. A double exponential function was used to fit each transient, and the observed rate of the initial fast exponential phase was plotted as an increase in mantATP concentration to define the kinetics of ATP binding (Fig. 5, Scheme 1, and Table 1).

$$k_{obs} = k_{+3}[\mathrm{mantATP}] + k_{-3} \quad \text{(Eq. 4)}$$

The linear fit of the data to Equation 4 provided the second-order rate constant of mantATP binding k_{+3} and the off rate k_{-3}, as defined by the *y* intercept with $K_d = k_{-3}/k_{+3}$.

Pulse-Chase Kinetics of ATP Binding—The MT·KIF3AB complex was preformed and rapidly mixed in the KinTek chemical quenched-flow instrument with increasing concentrations of MgATP plus trace [α-^{32}P]ATP and 200 mM KCl (syringe concentration) as described previously (37–39). The reaction was subsequently chased with 30 mM non-radiolabeled MgATP plus 100 mM KCl (syringe concentrations) and allowed to proceed for 0.7 s (>10 ATP turnovers). Each reaction was expelled from the instrument into a 2.0-ml Eppendorf tube containing 100 μl of 24 N formic acid, which terminated the reaction and released any nucleotide at the active site. Thin layer chromatography was used to separate [α-^{32}P]ATP from the products [α-^{32}P]ADP + P_i, and these were quantified using Image Gauge version 4 software (FUJIFILM Science Laboratory) (39). This experimental design quantifies [α-^{32}P]ATP bound at the active site because during the time of the chase, the stably bound [α-^{32}P]ATP proceeds through ATP hydrolysis, and the high concentration of non-radiolabeled MgATP dilutes any weakly bound [α-^{32}P]ATP and [α-^{32}P]ATP in solution. Equation 5 was used to fit the individual transients representing the time course of ATP binding,

$$\mathrm{Product} = A_0(1 - \exp(-k_b t)) + k_{slow} t \quad \text{(Eq. 5)}$$

where A_0 is the amplitude of the initial exponential phase representing the concentration of stably bound [α-^{32}P]ATP that proceeded through ATP hydrolysis to form [α-^{32}P]ADP·P_i at the active site during the first ATP turnover, k_b is the observed rate of the initial exponential phase, and k_{slow} is the rate of subsequent ATP binding events and corresponding to steady-state ATP turnover with *t* as the time in seconds. As described previously (37, 38), the additional KCl added to the [α-^{32}P]ATP syringe and ATP chase syringe is a strategy used for processive kinesins to weaken rebinding of the motor head to the MT as it steps forward 16 nm to the next MT binding site. This technique leaves the first ATP turnover undisturbed while slowing the rate of subsequent turnovers and results in a better defined quantification of the kinetics of the first ATP turnover.

The observed rates of the initial exponential burst phase of each transient were plotted as a function of increasing ATP concentration, and the Equation 6 fit of the data provides the following,

$$k_{obs} = (K_3 k'_{+3}[\mathrm{ATP}]/(K_3[\mathrm{ATP}] + 1)) \quad \text{(Eq. 6)}$$

where K_3 represents the equilibrium association constant for formation of the collision complex, and k'_{+3} is the first-order rate constant for the ATP-promoted isomerization with $K_d = 1/K_3$ (see Fig. 6, Scheme 1, and Table 1).

Acid Quench Kinetics of ATP Hydrolysis—The MT·KIF3AB complex was preformed and rapidly mixed in the KinTek chemical quenched-flow instrument with increasing concentrations of MgATP plus trace [α-^{32}P]ATP and 200 mM KCl (syringe concentration), as described previously (37, 38). At varying times of incubation, the reaction was quenched with 24 N formic acid (syringe concentration), which terminated the reaction and released any nucleotide at the active site. The resulting products, [α-^{32}P]ADP and P_i, were separated from [α-^{32}P]ATP by thin layer chromatography and quantified. The concentration of [α-^{32}P]ADP product formed was plotted as a function of time, and the hyperbolic fit of the data provided the rate constant of ATP hydrolysis, k_{+4} (see Fig. 7, Scheme 1, and Table 1).

MT·KIF3AB Dissociation Kinetics—The preformed MT·KIF3AB complex was rapidly mixed in the stopped-flow instrument with increasing concentrations of ATP plus 200 mM KCl (syringe concentration), and turbidity ($\lambda_{ex} = 340$ nm) was monitored. The observed decrease in turbidity as a function of time represents KIF3AB detachment from the MT because the MT·KIF3AB complex has a greater mass than MTs without kinesin motors or KIF3AB in solution. A double exponential function was fit to each transient, and the observed rate of the initial fast phase was plotted as a function of ATP concentration. The hyperbolic fit of the data provided the maximum rate constant of MT·KIF3AB dissociation, k_{+5} (see Fig. 8, Scheme 1, and Table 1). To test the hypothesis that ATP hydrolysis must occur prior to KIF3AB detachment from the MT, as observed for other kinesins (34, 37, 38, 40, 41), the experiment was repeated with buffer and non-hydrolyzable or slowly hydrolyzable ATP analogs, AMPPNP or ATPγS, respectively.

RESULTS

The goal of this study was to characterize the presteady-state kinetics of the steps in the ATPase cycle of KIF3AB to define the key principles that underlie its processivity, to reveal similarities and differences when compared with homodimeric kinesins, and to gain insight to understand the physiological advantage of a heterodimeric kinesin motor for its cellular roles. Studies involving detailed kinetic investigation have previously been hindered because of the inability to engineer constructs

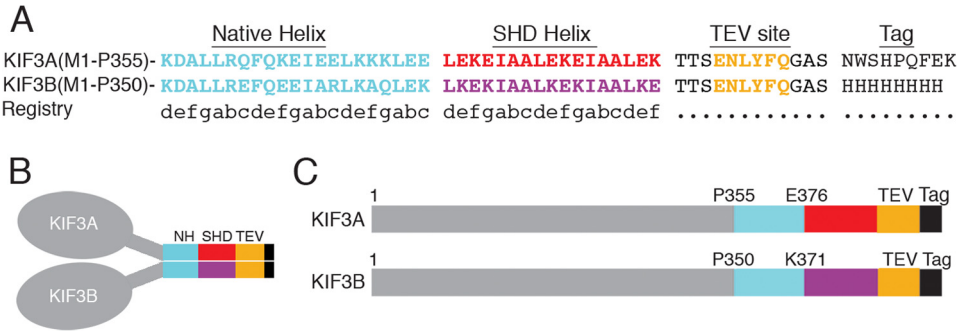

FIGURE 1. **KIF3AB motor design.** The KIF3AB heterodimer consists of the motor domain of KIF3A and KIF3B, followed by three heptads of native neck helix, a designed SHD followed by a flexible linker, a TEV proteolytic site, a flexible linker, and then the streptavidin or His_8 purification tag. *A*, amino acid sequence of either KIF3A or KIF3B showing the native helix (*cyan*), acidic SHD (*red*), basic SHD (*violet*), TEV site (*orange*) with the coiled-coiled registry based on the Paircoil2 analysis (49) of the neck and SHD helix domain. *B* and *C*, representations of the KIF3AB heterodimer with the motor head (*gray*), native helix (*cyan*), acidic SHD (*red*), basic SHD (*violet*), and TEV site (*orange*), with the purification tags in *black*. Images are not drawn to scale.

for large scale purification of soluble, well behaved heterodimers that represent the properties of the native KIF3AB motor. Plasmids for *KIF3A* and *KIF3B* were generated and co-expressed in *E. coli*. Both KIF3A and KIF3B contain the respective native sequence of its motor domain, neck linker, and three heptads of native coiled-coil sequence followed by the 17-amino acid residue SHD motif (Fig. 1). The purification strategy used a Ni^{2+}-NTA column to select for KIF3B-His_8, followed by a StrepTactin™ column to select for KIF3A-StrepII. This approach resulted in purification of KIF3AB heterodimers rather than homodimers of either KIF3AA or KIF3BB.

The analytical gel filtration results (Fig. 2*A*) and the SDS-polyacrylamide gel (Fig. 2*A*, *inset*) indicate that the truncated KIF3AB motor purified as a stable heterodimer. The Stokes radius for KIF3AB was calculated to be 4.7 nm, and the semilog plot of K_{av} *versus* M_r provided an apparent M_r of 98,500 Da, consistent with the molecular weight based on the amino acid sequence at 92,131 (Fig. 2, *B* and *C*). The protein yields were ~2.5 mg/g *E. coli* cell pellet. The motility experiments demonstrated that KIF3AB promoted robust MT plus-end-directed gliding at an average rate of 143 ± 1.9 nm/s (Fig. 2*D* and supplemental Video 1), and this MT gliding velocity predicts an ATP turnover rate of ~18 s^{-1} (143 nm/s/8-nm step with one ATP turnover/step). This MT gliding rate is somewhat slower than has been reported previously at 0.3–0.45 nm/s (2, 25), which we attribute to the more truncated kinesin-2 used in these studies, the buffer conditions, and the temperature of the assay.

Steady-state ATP Turnover—Steady-state experiments were used to probe KIF3AB ATPase kinetics. Fig. 3 shows representative steady-state experiments for KIF3AB. The ATPase parameters based on nine independent measurements (Table 1) were k_{cat} = 14.8 s^{-1}/nucleotide site (13.6–18.3 s^{-1}), $K_{m,ATP}$ = 118.3 μM (101.4–137.5 μM), and $K_{½,MT}$ = 0.12 μM (0.09–0.16 μM). These results indicate that the solution steady-state k_{cat} is consistent with that predicted from the MT gliding experiments. The $K_{m,ATP}$ was higher and more similar to *C. elegans* kinesin-2 at 280 μM (42) than determined previously for other processive kinesins, including kinesin-1 at 40–100 μM (43–47), kinesin-5 (Eg5) at 8 μM (48), and kinesin-7 (CENP-E) at 18 μM (36, 38) (Table 2).

Microtubule Association is Fast, Followed by MantADP Release at the Steady-state Rate—Historically, MT association kinetics were defined by measuring the change in turbidity as a function of time using the stopped-flow instrument because MT·KIF3AB complexes exhibit a higher turbidity signal than MTs without motors bound or kinesin motors free in solution. However, another strategy with much higher sensitivity is to use the fluorescence signal of mantADP release from the active sites of KIF3AB upon MT collision because at low MT concentrations, release of mantADP is limited by MT association. Fig. 4 shows the kinetics of mantADP release from KIF3AB after MT collision (E0-E1; Fig. 9). Representative transients of mantADP release at 15, 20, and 25 μM MTs are shown in Fig. 4*A*. Note that the transients are biphasic, and a double exponential fit provides the observed rate of the initial fast phase of mantADP release followed by a slower phase. When the observed rates of the initial phase for mantADP release were plotted as a function of MT concentration, the hyperbolic fit of the data provided the maximum rate constant k_{+2} at 12.8 s^{-1} (Fig. 4*B*, Scheme 1, and Table 1). At low concentrations of MTs, 0.5–1.5 μM MTs (Fig. 4*B*, *inset*), the data are linear because mantADP release is limited by MT collision. The fit of these data provided the second-order rate constant for MT association, k_{+1}, at 5.7 μM^{-1} s^{-1} (Scheme 1 and Table 1). Because the observed rate of mantADP release at 12.8 s^{-1} was similar to the steady-state k_{cat}, these results suggest that the rate-limiting step in the pathway may occur after MT collision and be limited by ADP release. The observed rates of the second phase of mantADP release were slow at 1–3 s^{-1} and significantly less than steady-state turnover and, therefore, are too slow to represent a step of the ATPase cycle. Consistent with this interpretation is the observation that the amplitude of mantADP release was predominantly associated with the initial fast phase at 67% of the amplitude (64–69%) with 33% (31–36%) of the amplitude associated with the second slow phase, suggesting that the rate constant for mantADP release at 12.8 s^{-1} represents the kinetics of MT collision of the first head followed by mantADP release.

MantATP Binding Kinetics—To measure the kinetics of ATP binding (E1-E2, Fig. 9), two experimental approaches were used. In the first, the fluorescence enhancement of mantATP

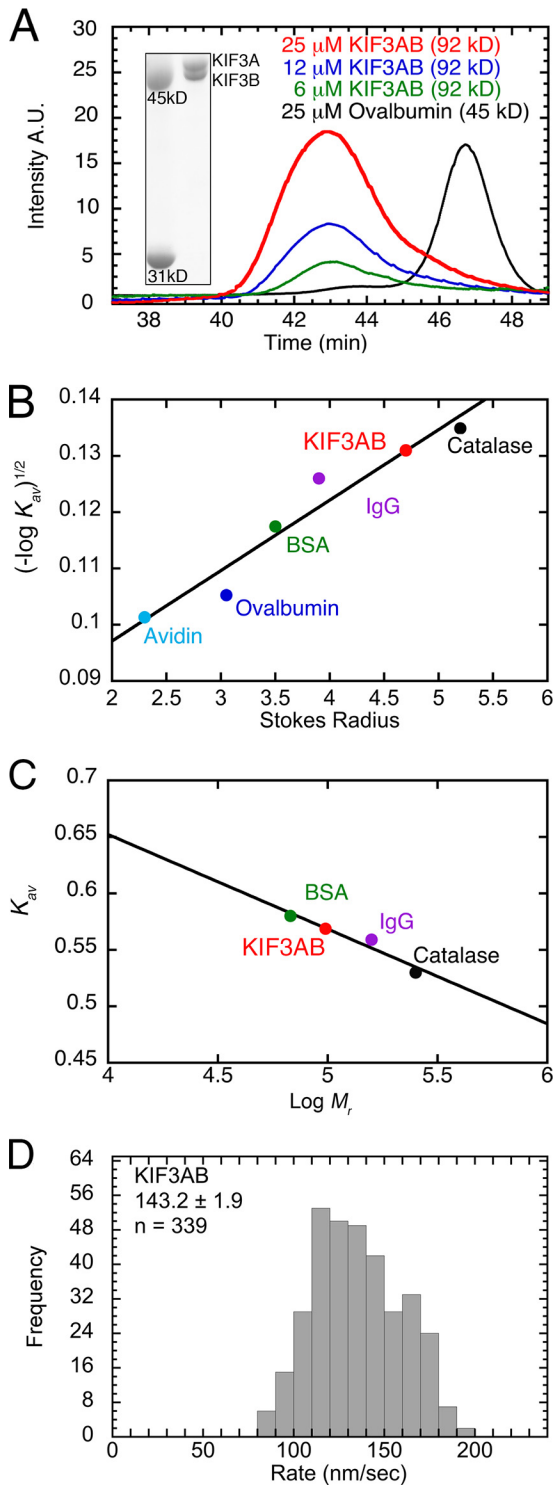

FIGURE 2. **KIF3AB characterization.** *A*, analytical HPLC gel filtration showing the elution of 6, 12, and 25 μM KIF3AB heterodimer (M_r = 92,131 Da) and 25 μM ovalbumin (M_r = 45,000 Da). *Inset*, 8% SDS-PAGE analysis of 2 μM KIF3AB motor stained with Coomassie Blue R-250. *Left lane*, M_r standards; *right lane*, KIF3AB showing KIF3A (M_r = 46,341 Da) and KIF3B (M_r = 45,790 Da). *B*, KIF3AB Stokes radius determination as described under "Experimental Procedures." KIF3AB R_S = 4.7 nm. *C*, apparent M_r of KIF3AB determined from the semilog plot of the partition coefficients of known standards *versus* log M_r. Apparent M_r of KIF3AB = 98.5 kDa. *D*, microtubule gliding assay. Rates of MT gliding were quantified as described previously (36). The histogram shows the distribution of observed rates with the mean at 143.2 ± 1.9 nm/s.

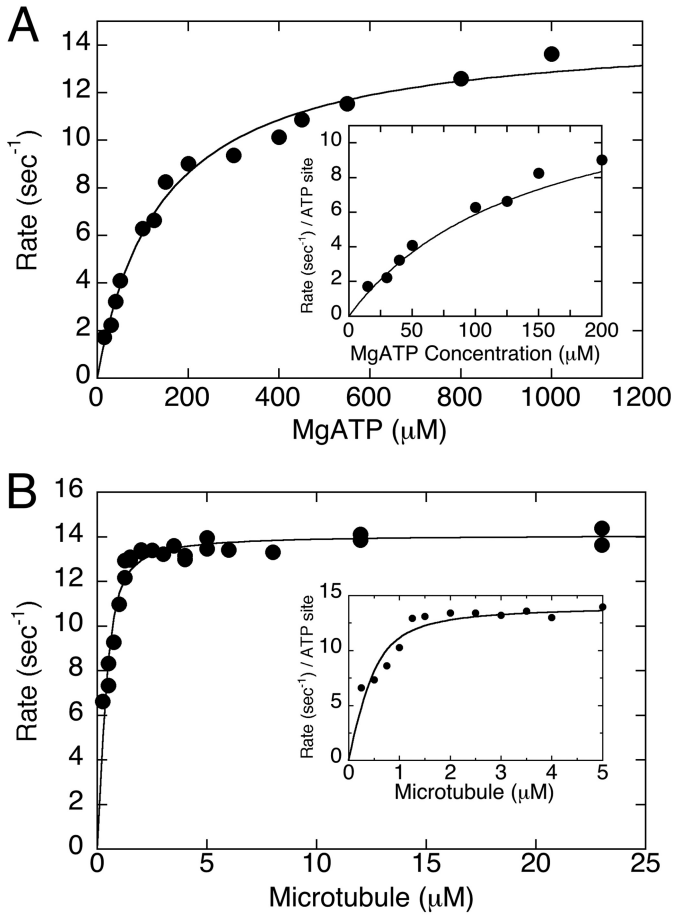

FIGURE 3. **Steady-state ATPase kinetics.** The MT·KIF3AB complex was rapidly mixed with [α-^{32}P]ATP. *A*, final concentrations: 0.5 μM KIF3AB nucleotide sites of ATP hydrolysis, 25 μM MTs, 15–1000 μM [α-^{32}P]ATP. The Michaelis-Menten fit of the data provided k_{cat} = 14.6 ± 0.4 s^{-1} per site and $K_{m,ATP}$ = 137.5 ± 13.2 μM. *B*, final concentrations: 0.5 μM KIF3AB nucleotide sites of ATP hydrolysis, 0.25–23 μM MTs, and 1 mM [α-^{32}P]ATP. Quadratic Equation 2 provided k_{cat} = 14.1 ± 0.2 s^{-1}/site and $K_{1/2,MT}$ = 0.14 ± 0.02 μM. *Insets*, the initial section of each curve is shown.

binding to the MT·KIF3AB complex was monitored (Fig. 5), and for the second, a pulse-chase approach with radiolabeled ATP was used (Fig. 6). For mantATP binding kinetics (Fig. 5), a MT·KIF3AB complex was preformed and rapidly mixed in the stopped-flow instrument with varying concentrations of mantATP. The transients in Fig. 5*A* show a biphasic fluorescence enhancement, and the double exponential fit of each transient reveals an initial fast phase of fluorescence enhancement followed by a slower phase. The observed rates from the initial fast phase of each transient were plotted as a function of mantATP concentration (Fig. 5*B*), and the linear fit of the data provided the second-order rate constant, k_{+3}, of mantATP binding at 7.5 μM^{-1} s^{-1} with the off rate, k_{-3}, at 46 s^{-1} (Scheme 1 and Table 1). Fig. 5*B* also presents the observed rates of the second slow phase for each transient as a function of mantATP concentration. These rates at 12–16 s^{-1} suggest that mantATP binding to the second head of KIF3AB is limited by the rate-limiting step of the pathway. In support of this hypothesis, the relative amplitude associated with each phase of the transient is approximately equal (initial phase 40–57% and second phase 43–58%). Therefore, these results support an alternating head

mechanism for ATP hydrolysis as observed for other processive kinesins. However, in the case of KIF3AB, it is unknown at this time whether the initial phase represents either KIF3A or KIF3B or a combination of each because of a 50–50 probability of either head colliding with the MT first.

Experiments were also performed with apyrase-treated MT·KIF3AB complexes (data not shown). These results were similar, with mantATP binding at 9.0 ± 0.03 μM^{-1} s^{-1} and the off rate k_{-3} at 65 ± 2.6 s^{-1}. The observed rates of the second slow phase of mantATP binding of each transient varied from 14 to 19 s^{-1}.

ATP Binding by Pulse-Chase—In the pulse-chase experimental design, the MT·KIF3AB complex was preformed and rapidly mixed in a chemical quenched-flow instrument with [α-^{32}P]ATP for 5–500 ms and subsequently chased with an excess of unlabeled MgATP for 0.7 s. During the ATP chase, unbound [α-^{32}P]ATP and weakly bound [α-^{32}P]ATP were diluted by the high concentration of unlabeled ATP. However, stably bound [α-^{32}P]ATP at the active site proceeds through ATP hydrolysis. Therefore, this experimental design quantifies the MT·KIF3AB·[α-^{32}P]ATP intermediate that proceeds through ATP hydrolysis. The individual transients in Fig. 6*A* are biphasic with an initial fast exponential phase of ATP bind-

TABLE 1
Kinesin-2 KIF3AB experimentally determined constants

MT KIF3AB·ADP association	k_{+1} = 5.7 ± 0.5 μM^{-1} s^{-1} k_{-1} = 0.3 ± 0.4 s^{-1}
MantADP release	k_{+2} = 12.8 ± 0.2 s^{-1} $K_{½,MTs}$ = 1.13 ± 0.08 μM
MantATP binding: first phase	k_{+3} = 7.5 ± 0.5 μM^{-1} s^{-1} k_{-3} = 46.1 ± 5.5 s^{-1} $K_{d,ATP}$ = 6.1 μM
MantATP binding: second phase	k_{obs} = 12–16 s^{-1}
ATP binding (pulse-chase)	K_3 = 0.16 ± 0.02 μM^{-1} k'_{+3} = 84.0 ± 1.9 s^{-1} $K_3k'_{+3}$ = 13.4 μM^{-1} s^{-1} $K_{d,ATP}$ = 6.4 μM A_0 = 3.2 ± 0.07 ADP·P_i/site
	$K_{d,ATP}$ = 76.7 ± 22.5 μM
ATP hydrolysis	k_{+4} = 33.0 ± 2.5 s^{-1} $K_{d,ATP}$ = 28.0 ± 7.0 μM A_0 = 3.0 ± 0.2 ADP·P_i/site
	$K_{d,ATP}$ = 50.1 ± 7.9 μM
MT·KIF3AB dissociation	k_{+5} = 22.3 ± 0.7 s^{-1} k_{-5} = 3.0 ± 0.6 s^{-1} $K_{½,ATP}$ = 133.0 ± 17.4 μM k_{on} = 0.09 ± 0.01 μM^{-1} s^{-1}
Steady-state parameters	k_{cat} = 14.8 ± 0.8 s^{-1} per site $K_{m,ATP}$ = 118 ± 7.7 μM $K_{½,MTs}$ = 0.12 ± 0.01 μM
MT gliding	143.2 ± 0.8 nm/s

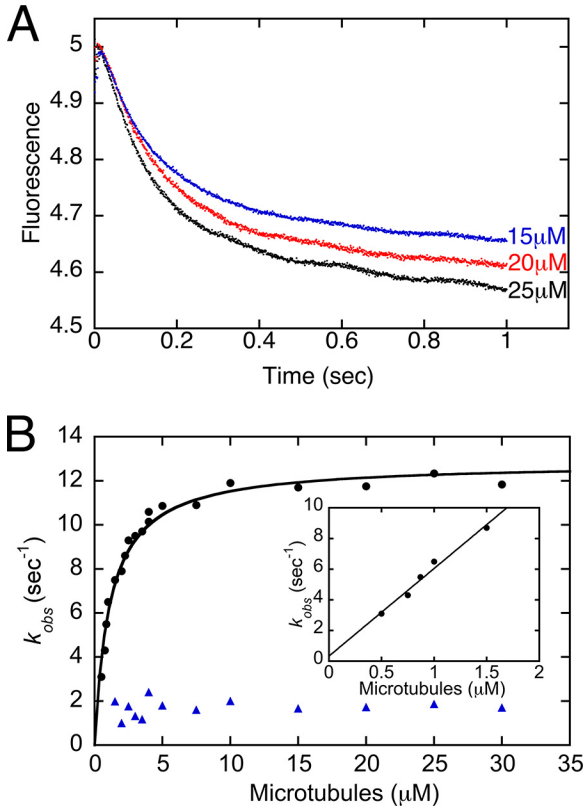

FIGURE 4. **MT association and mantADP release upon MT collision.** The KIF3AB·mantADP complex was preformed and rapidly mixed in the stopped-flow instrument with varying concentrations of MTs plus ATP. *A*, representative transients indicate a biphasic decrease in mantADP fluorescence as a function of time. Final concentrations were as follows: 2.5 μM KIF3AB nucleotide sites; 15 μM mantADP; 15, 20, and 25 μM MTs (*top* to *bottom*) with 1 mM MgATP. *B*, final concentrations: 1.0 μM KIF3AB nucleotide sites/3.75 μM mantADP for 0.5–1.5 μM MTs, 2.0 μM KIF3AB nucleotide sites/7.5 μM mantADP for 1.5–4 μM MTs, and 2.5 μM KIF3AB nucleotide sites/15 μM mantADP for 4–30 μM MTs plus 1 mM ATP (●). The hyperbolic fit of the data provided k_{+2} = 12.8 ± 0.2 s^{-1} and $K_{½,MT}$ = 1.13 ± 0.08 μM. *Inset*, at low MT concentrations, the linear increase in the observed rate of mantADP release represents the MT association kinetics because release of mantADP is limited by MT collision. The linear fit of these data provided the second-order rate constant k_{+1} = 5.7 ± 0.5 μM^{-1} s^{-1} and k_{-1} = 0.3 ± 0.4 s^{-1}. The second, slow phase of mantADP release (▲) was observed at rates ranging from 1.0 to 3.0 s^{-1}.

TABLE 2
Constants of processive kinesins

	Constants	KIF3AB	Kinesin-1[a]	Eg5-513[b]	CENP-E[c]
MT KIF3AB·ADP association	k_{+1}	5.7 $\mu M^{-1}s^{-1}$	11 $\mu M^{-1}s^{-1}$	2.8 $\mu M^{-1}s^{-1}$	0.08 $\mu M^{-1}s^{-1}$
	k_{-1}			10 s^{-1}	0.07 s^{-1}
MantADP release: first phase	k_{+2}	Head 1: 12.8 s^{-1}	Head 1: >200 s^{-1} Head 2: >100 s^{-1}	Head 1: 28 s^{-1} Head 2: ≫10 s^{-1}	Head 1: 0.9 s^{-1} Head 2: 19 s^{-1}
ATP binding	k_{+3}	7.5 $\mu M^{-1}s^{-1}$	2–5 $\mu M^{-1}s^{-1}$	5.8 $\mu M^{-1}s^{-1}$	1.4 $\mu M^{-1}s^{-1}$
	k'_{+3}	84.0 s^{-1}	240 s^{-1}	55 s^{-1}	48 s^{-1}
	$K_{d,ATP}$	6.4 μM	80 μM	9 μM	8 μM
	k_{-3}		120 s^{-1}	1–2 s^{-1}	
ATP hydrolysis	k_{+4}	33 s^{-1}	100–150 s^{-1}	10–12 s^{-1}	25 s^{-1}
MT·KIF3AB dissociation	k_{+5}	22.3 s^{-1}	40–60 s^{-1}	≫10 s^{-1}	1.4 s^{-1}
	$K_{½,ATP}$	133 μM	50 μM	6.9 μM	6.4 μM
MT-activated ATPase	k_{cat}	14.8 s^{-1}	50 s^{-1}	0.5–1 s^{-1}	0.9 s^{-1}
	$K_{m,ATP}$	118 μM	40–100 μM	8 μM	18 μM
	$K_{½,MTs}$	0.12 μM	0.9 μM	1.8 μM	1.5 μM
MT gliding		143 nm/s	0.5–0.8 nm/s	27–87 nm/s	11 nm/s

[a] Constants for dimeric kinesin-1 from *Drosophila*, rat, and human KHC expressed in *E. coli* (43, 45, 50–58).
[b] Constants for Eg5-513 are from Refs 48 and 59–63.
[c] Constants for CENP-E are from Refs. 36, 38, and 64.

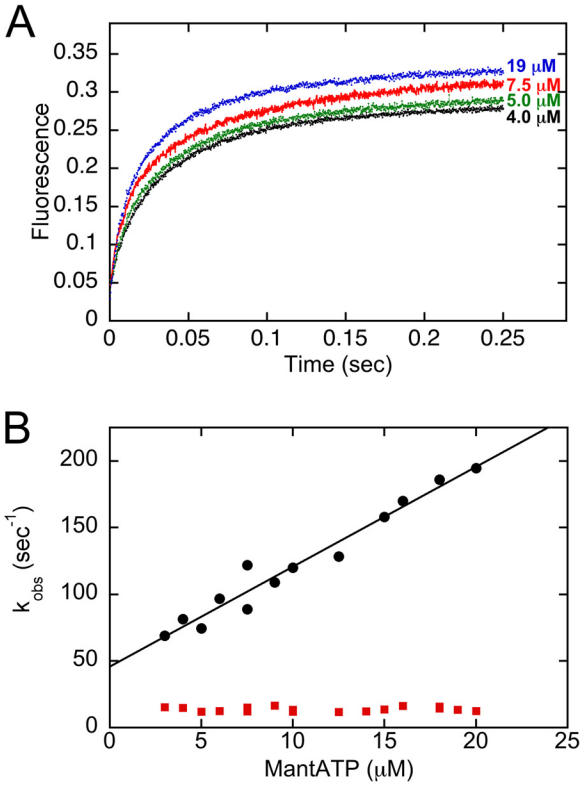

FIGURE 5. **MantATP binding kinetics.** The MT·KIF3AB complex was rapidly mixed in the stopped-flow instrument with increasing concentrations of mantATP. Final concentrations were as follows: 2.5 μM KIF3AB nucleotide sites, 7.5 μM MTs. *A*, representative transients at 4, 5, 7.5, and 19 μM mantATP show an exponential increase in fluorescence as a function of time. *B*, the observed rates of the initial exponential phase were plotted as a function of mantATP concentration (●), and the linear fit of the data provided k_{+3} = 7.5 ± 0.5 μM^{-1} s^{-1} and k_{-3} = 46.1 ± 5.5 s^{-1}. The second slow exponential phase (■) was observed at rates ranging between 12 and 16 s^{-1}.

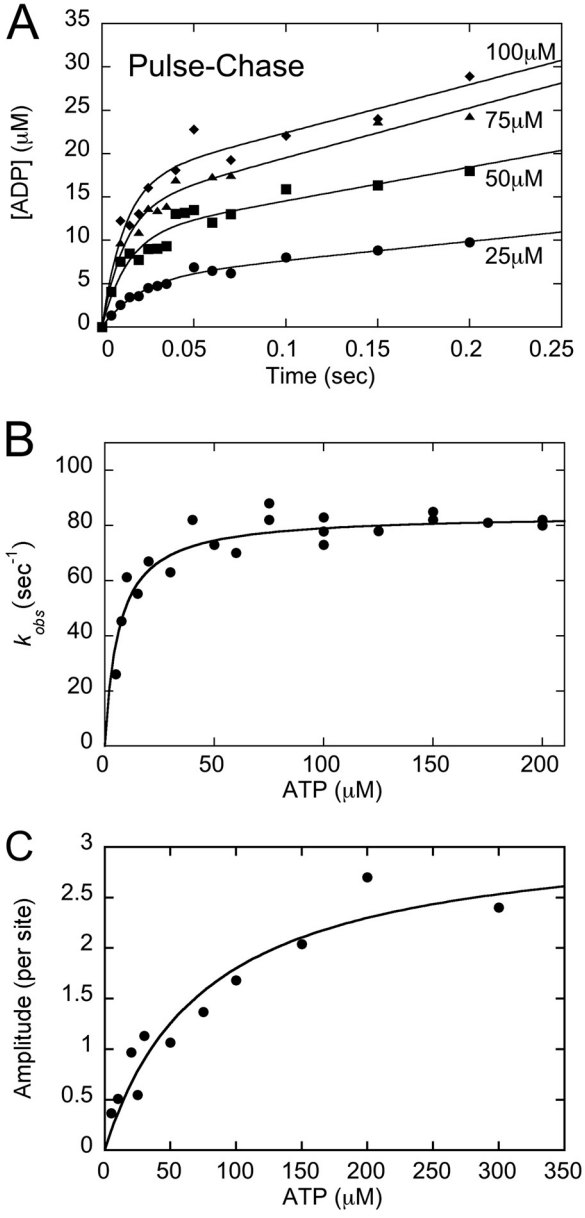

FIGURE 6. **Pulse-chase kinetics of ATP binding.** The MT·KIF3AB complex was rapidly mixed with increasing concentrations of [α-^{32}P]ATP + KCl in a chemical quenched-flow instrument and chased with 30 mM ATP + 100 mM KCl (syringe concentration). *A*, representative transients show the initial exponential formation of [α-^{32}P]ADP·P_i during the first ATP turnover, followed by a linear phase representing subsequent ATP turnovers. Final concentrations were as follows: 5 μM KIF3AB nucleotide sites, 20 μM MTs, 5–200 μM [α-^{32}P]ATP, and 100 mM KCl. *B*, the observed rates of the initial exponential phase were plotted as a function of ATP concentration, and Equation 6 provided K_3 = 0.16 ± 0.02 μM^{-1}, k'_{+3} = 84.0 ± 1.9 s^{-1}, and $K_{d,ATP}$ = 6.4 μM. Final concentrations were as follows: 5 μM KIF3AB nucleotide sites, 20 μM MTs, 5–200 μM [α-^{32}P]ATP, and 100 mM KCl or 10 μM KIF3AB nucleotide sites, 20 μM MTs, 5–200 μM [α-^{32}P]ATP, and 100 mM KCl. *C*, the amplitudes of the initial exponential burst phase were plotted as a function of ATP concentration, and the hyperbolic fit of the data provided A_0 = 3.2 ± 0.4 ADP·P_i/ATP site with an apparent $K_{d,ATP}$ = 76.7 ± 22.5 μM. Final concentrations were as follows: 5 μM KIF3AB, 20 μM MTs, 5–200 μM [α-^{32}P]ATP, 100 mM KCl or 10 μM KIF3AB, 20 μM MTs, 5–300 μM [α-^{32}P]ATP, and 100 mM KCl. Data shown in *B* and *C* are from multiple experiments.

ing that corresponds to the first ATP turnover, followed by a slower linear phase of ATP binding that corresponds to subsequent ATP binding events or steady-state activity. The fit of the data reveals that the observed rates of the initial exponential phase saturate rather than remaining linear, indicating that there is an ATP-dependent isomerization that occurred at the active site to generate the MT·KIF3AB*·ATP intermediate that is poised for ATP hydrolysis (Scheme 1 and Table 1). The maximum rate constant of the ATP-promoted isomerization, k'_{+3}, was 84 s^{-1}. The fit of the data to Equation 6 revealed that the apparent $K_{d,ATP}$ was 6.4 μM and similar to $K_{d,mantATP}$ at 6.1 μM (Table 1).

The amplitude of the initial exponential phase, which can be related to the concentration of ATP binding sites in the experiment, indicated a processive kinesin (Fig. 6) (45). The amplitude data in Fig. 6*C* were normalized to the concentration of KIF3AB nucleotide sites in the experiment and plotted as a function of ATP concentration. The maximum amplitude, A_0, was 3.2 ADP·P_i per nucleotide site, indicating that the KIF3AB heterodimer took, on average, three steps before detaching from the MT. The KIF3AB run length measured by the amplitude data from the pulse-chase experiments was shortened dramatically by the additional 100 mM KCl and buffer conditions of the experiment relative to run length results reported from single molecule experiments. Note too that the $K_{d,ATP}$ based on the amplitude data was higher at 76.7 μM.

ATP Hydrolysis Is Fast—The presteady-state kinetics of ATP hydrolysis (E4-E5; Fig. 9) were determined by rapidly mixing a

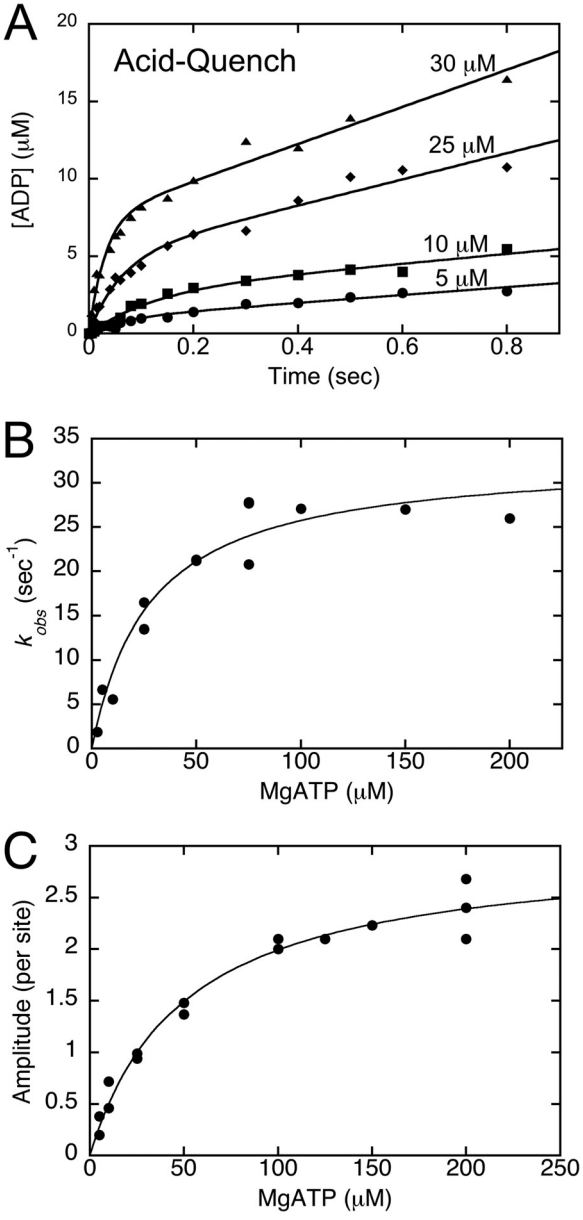

FIGURE 7. **Kinetics of ATP hydrolysis by acid quench.** The MT·KIF3AB complex was rapidly mixed with increasing concentrations of [α-^{32}P]ATP + KCl in a chemical quenched-flow instrument. The reaction was allowed to proceed for 5–800 ms and then quenched using formic acid. *A*, transients of 5, 10, 25, and 30 μM ATP show an exponential increase of [α-^{32}P]ADP·P$_i$ formed during the first ATP turnover, followed by a linear phase of product formation. Final concentrations were as follows: 5 μM KIF3AB nucleotide sites, 15 μM MTs, 5–200 μM [α-^{32}P]ATP, and 100 mM KCl. *B*, observed exponential product burst rates were plotted as a function of ATP concentration, and the fit of the data provided $k_{+4} = 33.0 \pm 2.5$ s^{-1} with $K_{d,ATP} = 28.0 \pm 7.0$ μM. Final concentrations were as follows: 8 μM KIF3AB nucleotide sites, 15 μM MTs, 5–200 μM [α-^{32}P]ATP, and 100 mM KCl or 5 μM KIF3AB nucleotide sites, 15 μM MTs, 25–200 μM [α-^{32}P]ATP, and 100 mM KCl. *C*, amplitudes of the initial exponential burst phase were plotted as a function of ATP concentration. The fit of the data indicates a maximum $A_0 = 3.0 \pm 0.2$ ADP·P$_i$/ATP site with $K_{d,ATP} = 50.1 \pm 7.9$ μM. Final concentrations were as follows: 8 μM KIF3AB nucleotide sites, 15 μM MTs, 5–200 μM [α-^{32}P]ATP, and 100 mM KCl or 5 μM KIF3AB nucleotide sites, 15 μM MTs, 25–200 μM [α-^{32}P]ATP, and 100 mM KCl. Data shown in *B* and *C* are from multiple experiments.

preformed MT·KIF3AB complex with varying concentrations of [α-^{32}P]ATP, followed by an acid quench to terminate the reaction and release any nucleotide from the active sites (Fig. 7). Transients of the time course of ATP hydrolysis are biphasic with an initial exponential phase that represents the rapid formation of ADP·P$_i$ on the active site during the first ATP turnover. A linear phase of product formation follows, which corresponds to subsequent ATP turnovers and therefore steady-state activity (Fig. 7*A*). The biphasic transients indicate that a slow step occurred after ATP hydrolysis. Fig. 7*B* is the plot of the observed rates of the initial exponential phase as a function of increasing ATP concentration, and the fit of the data provides the maximum rate constant of ATP hydrolysis, k_{+4}, at 33 s^{-1} with the $K_{d,ATP}$ at 28 μM. Fig. 7*C* shows the plot of the amplitudes of the initial exponential phase as a function of ATP concentration, which can be correlated with the concentration of active sites in the experiment. The fit of the data provided the maximum amplitude at 3.0 ADP·P$_i$/nucleotide site, suggesting that the KIF3AB heterodimer took on average three steps prior to detaching from the MT, each requiring one ATP turnover. The $K_{d,ATP}$ values based on the amplitude data were higher at 50.1 μM. Note too that the observation that the relative amplitudes in the pulse-chase and ATP hydrolysis experiments were similar is consistent with the hypothesis that there were not significant reversals at ATP binding (Scheme 1, *steps 3* and *3′*).

MT·KIF3AB Dissociation Kinetics Reveal an Unusual ATP Dependence—To evaluate the kinetics of KIF3AB detachment from the MT (E5-E6; Fig. 9), an MT·KIF3AB complex was preformed and rapidly mixed in the stopped-flow instrument with ATP, and the turbidity signal was monitored (Fig. 8). Most kinesins examined to date show that ATP binding and ATP hydrolysis are required prior to motor detachment from the MT. When the dissociation kinetics experiments were performed with ATP, the transients revealed a significant decrease in turbidity as the motors dissociate into the solution, as expected (Fig. 8A). In contrast, when the experiment was repeated with buffer, the non-hydrolyzable (AMPPNP) or slowly hydrolyzable (ATPγS) ATP analogs, the turbidity signal remained flat with little change as a function of time. These results indicate that ATP hydrolysis is required prior to KIF3AB detachment from the MT.

When the dissociation kinetics were repeated as a function of ATP concentration, there was an increase in the observed rate of KIF3AB detachment from the MT as a function of ATP concentration (Fig. 8*B*). The hyperbolic fit of the data provided the maximum rate constant of dissociation, k_{+5}, at 22.3 s^{-1} with the $K_{½,ATP}$ at 133 μM (Scheme 1 and Table 1). The apparent weak binding of ATP was very surprising and was not seen at this step for other processive kinesins (36, 43, 45, 48). The *inset* in Fig. 8*B* shows the observed rates of dissociation at low concentrations of MgATP, and the fit of the data provides an apparent second-order rate constant at 0.09 μM^{-1} s^{-1}. At low ATP concentrations, the data should represent ATP binding because KIF3AB dissociation at low ATP concentrations is limited by ATP binding and ATP hydrolysis, both of which are fast steps. Note that the steady-state ATPase experiments also showed a weak $K_{m,ATP}$ at 118.3 μM.

DISCUSSION

The heterodimeric KIF3AB is a highly processive motor that results from two independent gene products. These studies identify three key characteristics in the mechanochemical cycle

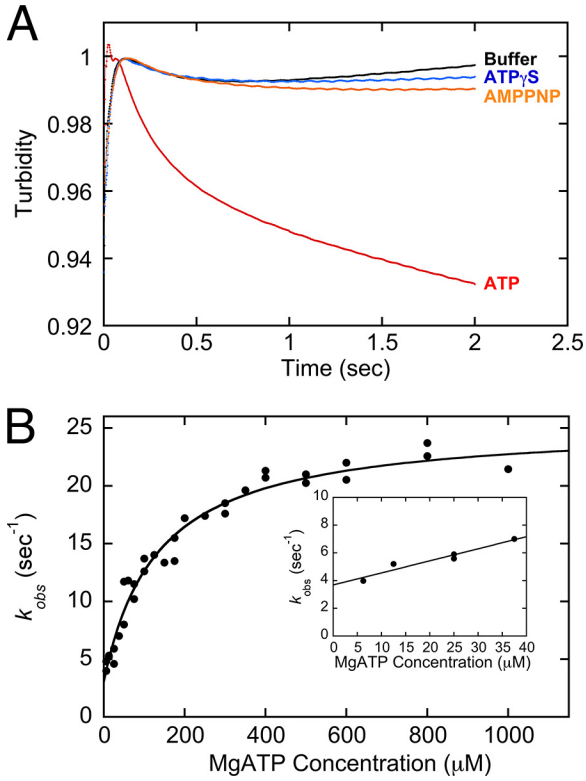

FIGURE 8. **ATP-promoted dissociation of the MT·KIF3AB complex.** *A*, final concentrations: 2 μM KIF3AB nucleotide sites, 7.5 μM MTs, 0.5 mM ATP or ATP analog, and 100 mM KCl. Shown is a comparison of dissociation kinetics in the presence of buffer, AMPPNP, ATPγS, and ATP. *B*, the preformed MT·KIF3AB complex was rapidly mixed in the stopped-flow instrument with increasing concentrations of ATP plus KCl. Final concentrations were as follows: 4.5 μM KIF3AB nucleotide sites, 5 μM MTs, 0–1000 μM ATP with 100 mM KCl. The observed rates of the initial exponential phase were plotted as a function of MgATP concentration. The hyperbolic fit of the data provides $k_{+5} = 22.3 \pm 0.7\ s^{-1}$, $k_{-5} = 3.0 \pm 0.6\ s^{-1}$, and $K_{1/2,ATP} = 133.0 \pm 17.4\ \mu M$. *Inset*, a linear fit from 0 to 37.5 μM MgATP defined an apparent second-order rate constant at $0.09 \pm 0.01\ \mu M^{-1}\ s^{-1}$.

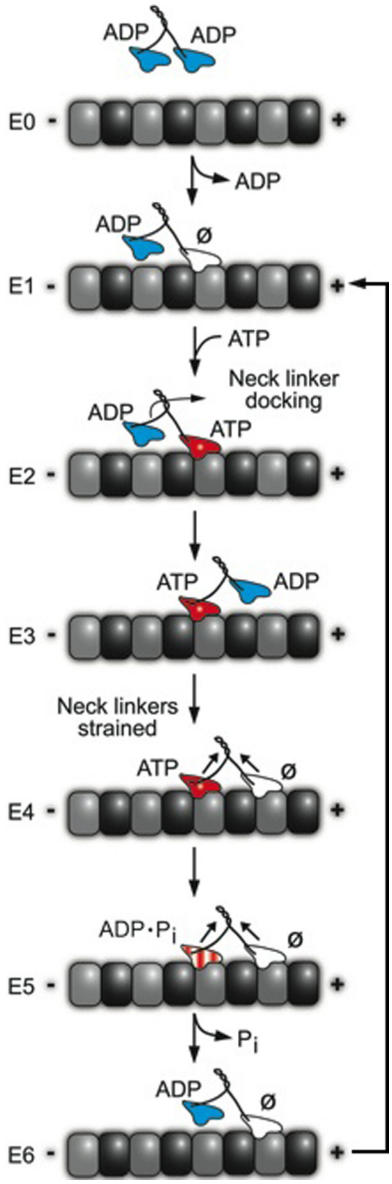

FIGURE 9. **Stepping model for KIF3AB.** The processive run begins upon MT collision by KIF3AB·ADP, followed by ADP release (E1). The leading head is now nucleotide-free with the trailing head detached and ADP tightly bound. ATP binding at the leading head promotes a series of conformational changes, including neck linker docking and movement of the rearward head forward to its next MT binding site, resulting in ADP release (E2-E4). Intermolecular strain between the heads is generated in the E4 intermediate prohibiting ATP binding to the nucleotide-free leading head. The strain is relieved after the trailing head undergoes ATP hydrolysis followed by phosphate release. This trailing head is now ADP-bound and has a weak affinity for MTs (E5-E6). ATP binding at the leading head of E6 initiates the cycle to repeat without detachment from the MT. In this model, there is an alternating ATPase cycle for KIF3A followed by KIF3B, but it is currently unknown which head collides with the MT first.

of KIF3AB: a rate-limiting step attributed to ADP release after MT collision, a relatively slow MT·KIF3AB dissociation at 22.3 s^{-1} that may be limiting the rate of stepping, and an apparent weak $K_{m,ATP}$ revealed by the MT·KIF3AB dissociation kinetics and steady-state ATP turnover. These three distinctive characteristics indicate that KIF3AB is tuned differently from other homodimeric processive motors (Table 2). This implies that the mechanochemical cycle of KIF3AB could contribute to its niche role in assembly and maintenance of cilia and flagella and its other kinesin-2 transport functions.

Key Principles for KIF3AB—The results presented suggest that KIF3AB shares key characteristics that are common to processive kinesins although each belongs to a different subfamily. Processive kinesins use an asymmetric hand-over-hand mechanism that requires coordination of the ATPase cycles to decrease the probability that both heads will enter an MT weakly bound state simultaneously, and for each, a processive step is tightly coupled to one ATP turnover per 8-nm step. Like conventional kinesin and CENP-E, KIF3AB holds ADP tightly in solution at each active site, and collision with the MT activates ADP release to begin the processive run. ATP binding provides the free energy required to drive the structural transitions for MT plus-end-directed motion, where the neck linker plays a key role through docking onto the catalytic core. The docking causes the detachment of the trailing ADP head, which steps forward to find the next MT binding site 16 nm toward the MT plus end. Head-head coordination between KIF3A and KIF3B is mediated in part through nucleotide state but also through intermolecular strain defined in part by the length and charged residues of the neck linker. Using these key principles along with the experimental rate and equilibrium constants summarized in Table 1, a stepping model is proposed in Fig. 9.

A Model for KIF3AB Processive Stepping—The proposed model (Fig. 9) starts with cytosolic KIF3AB tightly bound with ADP at each head. MT collision occurs as a fast step at 5.7 μM^{-1} s^{-1} (Fig. 4), followed by rate-limiting ADP release at 12.8 s^{-1} (Fig. 4). The leading head of the E1 intermediate is tightly bound to the MT and nucleotide-free with the trailing head of the E1 intermediate detached from the MT with ADP tightly bound. Note that the ATPase cycles within the KIF3AB dimer are now out of phase with each other and must remain coordinated to sustain the processive run. ATP binding at the leading head (E2) is also a fast step at 7.5 μM^{-1} s^{-1} (Fig. 5) followed by an ATP-promoted isomerization at 84 s^{-1} (Fig. 6) to form the intermediate poised for ATP hydrolysis (E4). ATP hydrolysis is also rapid at 33 s^{-1} (Fig. 7) followed by phosphate release and detachment of the trailing head at 22.3 s^{-1} (Fig. 8), completing one ATP turnover. The intermediate at E6 is poised to bind ATP at its leading head to begin the second ATP turnover but now on the alternate head.

The results for KIF3AB suggest that there are two key steps in the ATPase cycle that modulate interactions with the MT and control the overall cycle (Table 1). The initial MT collision coupled with ADP release was the slowest step measured at 12.8 s^{-1}, yet ATP-promoted MT·KIF3AB dissociation was also slow at 22.3 s^{-1}. The steady-state k_{cat} at 14.8 s^{-1} is more similar to the rate constant of ADP release after MT collision; however, the MT gliding velocity at 143 nm/s or at 18 s^{-1} suggests that possibly phosphate release coupled to detachment of the KIF3AB·ADP trailing head at E5-E6 also contributes to or controls the overall stepping rate.

The mantATP binding kinetics in Fig. 5 reveal a 12–16 s^{-1} event that must occur prior to mantATP binding to the second head (*i.e.* the leading nucleotide-free head at E6). This event may represent ADP release from the new leading head at the E3-E4 transition, provided that ADP release occurs at a similar rate as observed for the MT collision step at E1. Once both heads are tightly bound at E4, strain develops between the two heads and is mediated by the coiled-coil and neck linkers, which potentially triggers ATP hydrolysis (E4-E5). Note that this model does not distinguish between phosphate release and KIF3AB dissociation from E5-E6. For the processive kinesins, these two steps are thought to be coupled where phosphate release occurs first, followed by motor head detachment in the weak MT binding ADP-bound state, with one step being fast and the other slow such that only the slow step is observed experimentally. For kinesin-1 using a mutant that stalled on the MT, it was shown that phosphate release was the slow rate-limiting step, followed by rapid dissociation (47).

MT·KIF3AB Dissociation Kinetics Reveal an Unusual ATP Dependence—The dissociation kinetics (Fig. 8) were surprising because of the relatively high $K_{½,ATP}$ at 133 μM and ranging from 117 to 208 μM in multiple experiments. The apparent weaker ATP affinity at this step was not observed for the other processive kinesins, including kinesin-1, kinesin-5 (Eg5), or kinesin-7 (CENP-E) (Table 2) (38, 45, 48), and it is unclear what its contribution is to the KIF3AB motor behavior. Because the dissociation experimental design begins with an MT·KIF3AB complex much like the experiments to measure ATP hydrolysis, the dissociation kinetics may represent approximately three ATP turnovers before KIF3AB detachment from the MT. Therefore, the weak $K_{½,ATP}$ may represent an accumulation of multiple steps. However, the equilibrium dissociation constants for KIF3AB ATP binding and hydrolysis are similar to those for kinesin-1 measured previously, and kinesin-1 does not exhibit this apparent weak ATP affinity (Table 2). One interpretation is that the weak ATP affinity is related to the longer neck linker extension in KIF3AB that alters the intermolecular communication between the motor heads that results in shorter processive run lengths. Shastry and Hancock (26) showed that the run lengths of kinesin-1, -2, -3, -5, and -7 motors scaled inversely with neck linker length, suggesting that interhead tension determines processivity for diverse N-terminal kinesins. However, both CENP-E and Eg5 have neck linkers of 18 amino acid residues and are more similar to KIF3AB at 17 residues, yet both CENP-E and Eg5 show relatively tight ATP affinity at the dissociation step at 6.4 and 6.9 μM, respectively (38, 48) (Table 2). Moreover, a similar $K_{m,ATP}$ for KIF3AB was also detected in the steady-state ATPase experiments at 118.3 μM (Fig. 3 and Table 1), suggesting that this is a novel characteristic of KIF3AB, and experiments are under way to understand the source of this apparent weak $K_{m,ATP}$ and its role in KIF3AB processive stepping.

Initiation of the Processive Run—The KIF3AB heterodimer is composed of two motor heads with 86% sequence similarity, which raises the question of whether there is a preferential binding of one head over the other in initiating the processive run. As such, does KIF3AB rely on MT collision to determine the leading head, or is there an intrinsic asymmetry within the KIF3AB heterodimer that favors one motor head over the other for the first step of the processive run? The model as proposed in Fig. 9 makes no assumption about whether KIF3A or KIF3B collides with the MT initially or, alternatively, whether it is a mixed population in the solution experiments. Further, KIF3AB initiates the processive run with a slow ADP release step at E0-E1 (Fig. 9), but it is not obvious at this time whether ADP release at 12.8 s^{-1} at each subsequent step limits the overall rate of stepping or whether once the processive run begins that it is phosphate release coupled to rearward head detachment that limits processive stepping (E5-E6; Fig. 9). Data in support of the latter argument are the similarity in rate constants: steady-state k_{cat} at 14.6 s^{-1}, MT·KIF3AB dissociation at 22.3 s^{-1}, and MT gliding at 18 s^{-1}. Because the conditions of the kinetic experiments reported limit a processive run to approximately three steps before detachment, rate-limiting ADP release may have a greater influence in the kinetics than in a single molecule experiment whose conditions favor longer processive runs.

Why KIF3AB Heterodimerization—This initial study for KIF3AB has set the stage for the upcoming experiments to answer the many intriguing questions to understand the tuning of KIF3AB for its unique transport roles in the highly crowded environment of cilia and flagella. The shorter run lengths characteristic of KIF3AB and other heterotrimeric kinesin-2s and defined by their structure and mechanochemistry suggest that there is a physiological advantage of these motor properties that has persisted evolutionarily. We propose that because there are multiple kinesin-2 motors per intraflagellar transport particle

and the transport distance is shorter within cilia at 1–10 μm, there may not be a functional requirement for greater processivity. In fact, the motor characteristics of KIF3AB may enable kinesin-2 to navigate obstacles rather than stall as observed for more highly processive kinesins and myosins. The critical steps in the pathway that most impact the degree of processivity are E2-E4 and E4-E5 (Fig. 9) because these are the critical points that maintain the ATPase cycle on each head out of phase with each other. Therefore, the key mechanistic questions ahead are to understand the properties specifically of KIF3A and KIF3B and how their heterodimerization influences the intermolecular communication to control the processivity of KIF3AB.

Acknowledgments—We thank Dr. Stephanie Guzik-Lendrum, Brandon Bensel, and Rebecca Phillips for critical reading and discussion.

REFERENCES

1. Cole, D. G., Diener, D. R., Himelblau, A. L., Beech, P. L., Fuster, J. C., and Rosenbaum, J. L. (1998) *Chlamydomonas* kinesin-II-dependent intraflagellar transport (IFT): IFT particles contain proteins required for ciliary assembly in *Caenorhabditis elegans* sensory neurons. *J. Cell Biol.* **141,** 993–1008
2. Yamazaki, H., Nakata, T., Okada, Y., and Hirokawa, N. (1995) KIF3A/B: a heterodimeric kinesin superfamily protein that works as a microtubule plus end-directed motor for membrane organelle transport. *J. Cell Biol.* **130,** 1387–1399
3. Vernos, I., Heasman, J., and Wylie, C. (1993) Multiple kinesin-like transcripts in *Xenopus* oocytes. *Dev. Biol.* **157,** 232–239
4. Stewart, R. J., Pesavento, P. A., Woerpel, D. N., and Goldstein, L. S. (1991) Identification and partial characterization of six members of the kinesin superfamily in *Drosophila*. *Proc. Natl. Acad. Sci. U.S.A.* **88,** 8470–8474
5. Tuma, M. C., Zill, A., Le Bot, N., Vernos, I., and Gelfand, V. (1998) Heterotrimeric kinesin II is the microtubule motor protein responsible for pigment dispersion in *Xenopus* melanophores. *J. Cell Biol.* **143,** 1547–1558
6. Aizawa, H., Sekine, Y., Takemura, R., Zhang, Z., Nangaku, M., and Hirokawa, N. (1992) Kinesin family in murine central nervous system. *J. Cell Biol.* **119,** 1287–1296
7. Kondo, S., Sato-Yoshitake, R., Noda, Y., Aizawa, H., Nakata, T., Matsuura, Y., and Hirokawa, N. (1994) KIF3A is a new microtubule-based anterograde motor in the nerve axon. *J. Cell Biol.* **125,** 1095–1107
8. Henson, J. H., Cole, D. G., Terasaki, M., Rashid, D., and Scholey, J. M. (1995) Immunolocalization of the heterotrimeric kinesin-related protein KRP(85/95) in the mitotic apparatus of sea urchin embryos. *Dev. Biol.* **171,** 182–194
9. Pesavento, P. A., Stewart, R. J., and Goldstein, L. S. (1994) Characterization of the KLP68D kinesin-like protein in *Drosophila*: possible roles in axonal transport. *J. Cell Biol.* **127,** 1041–1048
10. Shakir, M. A., Fukushige, T., Yasuda, H., Miwa, J., and Siddiqui, S. S. (1993) *C. elegans* osm-3 gene mediating osmotic avoidance behaviour encodes a kinesin-like protein. *Neuroreport* **4,** 891–894
11. Wedaman, K. P., Meyer, D. W., Rashid, D. J., Cole, D. G., and Scholey, J. M. (1996) Sequence and submolecular localization of the 115-kD accessory subunit of the heterotrimeric kinesin-II (KRP85/95) complex. *J. Cell Biol.* **132,** 371–380
12. Cole, D. G., Chinn, S. W., Wedaman, K. P., Hall, K., Vuong, T., and Scholey, J. M. (1993) Novel heterotrimeric kinesin-related protein purified from sea urchin eggs. *Nature* **366,** 268–270
13. Gumy, L. F., Chew, D. J., Tortosa, E., Katrukha, E. A., Kapitein, L. C., Tolkovsky, A. M., Hoogenraad, C. C., and Fawcett, J. W. (2013) The kinesin-2 family member KIF3C regulates microtubule dynamics and is required for axon growth and regeneration. *J. Neurosci.* **33,** 11329–11345
14. Yang, Z., and Goldstein, L. S. (1998) Characterization of the KIF3C neural kinesin-like motor from mouse. *Mol. Biol. Cell* **9,** 249–261
15. Scholey, J. M. (2013) Kinesin-2: a family of heterotrimeric and homodimeric motors with diverse intracellular transport functions. *Annu. Rev. Cell Dev. Biol.* **29,** 443–469
16. Ishikawa, H., and Marshall, W. F. (2011) Ciliogenesis: building the cell's antenna. *Nat. Rev. Mol. Cell Biol.* **12,** 222–234
17. Verhey, K. J., Kaul, N., and Soppina, V. (2011) Kinesin assembly and movement in cells. *Annu. Rev. Biophys.* **40,** 267–288
18. Marszalek, J. R., Liu, X., Roberts, E. A., Chui, D., Marth, J. D., Williams, D. S., and Goldstein, L. S. (2000) Genetic evidence for selective transport of opsin and arrestin by kinesin-II in mammalian photoreceptors. *Cell* **102,** 175–187
19. Takeda, S., Yamazaki, H., Seog, D. H., Kanai, Y., Terada, S., and Hirokawa, N. (2000) Kinesin superfamily protein 3 (KIF3) motor transports fodrin-associating vesicles important for neurite building. *J. Cell Biol.* **148,** 1255–1265
20. Nonaka, S., Tanaka, Y., Okada, Y., Takeda, S., Harada, A., Kanai, Y., Kido, M., and Hirokawa, N. (1998) Randomization of left-right asymmetry due to loss of nodal cilia generating leftward flow of extraembryonic fluid in mice lacking KIF3B motor protein. *Cell* **95,** 829–837
21. Takeda, S., Yonekawa, Y., Tanaka, Y., Okada, Y., Nonaka, S., and Hirokawa, N. (1999) Left-right asymmetry and kinesin superfamily protein KIF3A: new insights in determination of laterality and mesoderm induction by kif3A$^{-/-}$ mice analysis. *J. Cell Biol.* **145,** 825–836
22. Marszalek, J. R., Ruiz-Lozano, P., Roberts, E., Chien, K. R., and Goldstein, L. S. (1999) Situs inversus and embryonic ciliary morphogenesis defects in mouse mutants lacking the KIF3A subunit of kinesin-II. *Proc. Natl. Acad. Sci. U.S.A.* **96,** 5043–5048
23. Rogers, S. L., Tint, I. S., Fanapour, P. C., and Gelfand, V. I. (1997) Regulated bidirectional motility of melanophore pigment granules along microtubules in vitro. *Proc. Natl. Acad. Sci. U.S.A.* **94,** 3720–3725
24. Cole, D. G., Cande, W. Z., Baskin, R. J., Skoufias, D. A., Hogan, C. J., and Scholey, J. M. (1992) Isolation of a sea urchin egg kinesin-related protein using peptide antibodies. *J. Cell Sci.* **101,** 291–301
25. Muthukrishnan, G., Zhang, Y., Shastry, S., and Hancock, W. O. (2009) The processivity of kinesin-2 motors suggests diminished front-head gating. *Curr. Biol.* **19,** 442–447
26. Shastry, S., and Hancock, W. O. (2010) Neck linker length determines the degree of processivity in kinesin-1 and kinesin-2 motors. *Curr. Biol.* **20,** 939–943
27. Brunnbauer, M., Mueller-Planitz, F., Kösem, S., Ho, T. H., Dombi, R., Gebhardt, J. C., Rief, M., and Okten, Z. (2010) Regulation of a heterodimeric kinesin-2 through an unprocessive motor domain that is turned processive by its partner. *Proc. Natl. Acad. Sci. U.S.A.* **107,** 10460–10465
28. Schroeder, H. W., 3rd, Hendricks, A. G., Ikeda, K., Shuman, H., Rodionov, V., Ikebe, M., Goldman, Y. E., and Holzbaur, E. L. (2012) Force-dependent detachment of kinesin-2 biases track switching at cytoskeletal filament intersections. *Biophys. J.* **103,** 48–58
29. Brunnbauer, M., Dombi, R., Ho, T. H., Schliwa, M., Rief, M., and Ökten, Z. (2012) Torque generation of kinesin motors is governed by the stability of the neck domain. *Mol. Cell* **46,** 147–158
30. Klenchin, V. A., Frye, J. J., Jones, M. H., Winey, M., and Rayment, I. (2011) Structure-function analysis of the C-terminal domain of CNM67, a core component of the *Saccharomyces cerevisiae* spindle pole body. *J. Biol. Chem.* **286,** 18240–18250
31. Zhang, Y., and Hancock, W. O. (2004) The two motor domains of KIF3A/B coordinate for processive motility and move at different speeds. *Biophys. J.* **87,** 1795–1804; Correction (2008) *Biophys. J.* **95,** 3521
32. Lindhout, D. A., Litowski, J. R., Mercier, P., Hodges, R. S., and Sykes, B. D. (2004) NMR solution structure of a highly stable *de novo* heterodimeric coiled-coil. *Biopolymers* **75,** 367–375
33. Rank, K. C., Chen, C. J., Cope, J., Porche, K., Hoenger, A., Gilbert, S. P., and Rayment, I. (2012) Kar3Vik1, a member of the kinesin-14 superfamily, shows a novel kinesin microtubule binding pattern. *J. Cell Biol.* **197,** 957–970
34. Cochran, J. C., Krzysiak, T. C., and Gilbert, S. P. (2006) Pathway of ATP hydrolysis by monomeric kinesin Eg5. *Biochemistry* **45,** 12334–12344
35. Patel, S. S., and Hingorani, M. M. (1993) Oligomeric structure of bacteriophage T7 DNA primase/helicase proteins. *J. Biol. Chem.* **268,**

10668–10675
36. Sardar, H. S., Luczak, V. G., Lopez, M. M., Lister, B. C., and Gilbert, S. P. (2010) Mitotic kinesin CENP-E promotes microtubule plus-end elongation. *Curr. Biol.* **20,** 1648–1653
37. Chen, C. J., Rayment, I., and Gilbert, S. P. (2011) Kinesin Kar3Cik1 ATPase pathway for microtubule cross-linking. *J. Biol. Chem.* **286,** 29261–29272
38. Sardar, H. S., and Gilbert, S. P. (2012) Microtubule capture by mitotic kinesin centromere protein E (CENP-E). *J. Biol. Chem.* **287,** 24894–24904
39. Gilbert, S. P., and Mackey, A. T. (2000) Kinetics: a tool to study molecular motors. *Methods* **22,** 337–354
40. Chen, C. J., Porche, K., Rayment, I., and Gilbert, S. P. (2012) The ATPase pathway that drives the kinesin-14 Kar3Vik1 powerstroke. *J. Biol. Chem.* **287,** 36673–36682
41. Foster, K. A., Mackey, A. T., and Gilbert, S. P. (2001) A mechanistic model for Ncd directionality. *J. Biol. Chem.* **276,** 19259–19266
42. Pan, X., Ou, G., Civelekoglu-Scholey, G., Blacque, O. E., Endres, N. F., Tao, L., Mogilner, A., Leroux, M. R., Vale, R. D., and Scholey, J. M. (2006) Mechanism of transport of IFT particles in *C. elegans* cilia by the concerted action of kinesin-II and OSM-3 motors. *J. Cell Biol.* **174,** 1035–1045
43. Auerbach, S. D., and Johnson, K. A. (2005) Alternating site ATPase pathway of rat conventional kinesin. *J. Biol. Chem.* **280,** 37048–37060
44. Skiniotis, G., Cochran, J. C., Müller, J., Mandelkow, E., Gilbert, S. P., and Hoenger, A. (2004) Modulation of kinesin binding by the C-termini of tubulin. *EMBO J.* **23,** 989–999
45. Gilbert, S. P., Webb, M. R., Brune, M., and Johnson, K. A. (1995) Pathway of processive ATP hydrolysis by kinesin. *Nature* **373,** 671–676
46. Klumpp, L. M., Brendza, K. M., Gatial, J. E., 3rd, Hoenger, A., Saxton, W. M., and Gilbert, S. P. (2004) Microtubule-kinesin interface mutants reveal a site critical for communication. *Biochemistry* **43,** 2792–2803
47. Klumpp, L. M., Hoenger, A., and Gilbert, S. P. (2004) Kinesin's second step. *Proc. Natl. Acad. Sci. U.S.A.* **101,** 3444–3449
48. Krzysiak, T. C., and Gilbert, S. P. (2006) Dimeric Eg5 maintains processivity through alternating-site catalysis with rate-limiting ATP hydrolysis. *J. Biol. Chem.* **281,** 39444–39454
49. McDonnell, A. V., Jiang, T., Keating, A. E., and Berger, B. (2006) Paircoil2: improved prediction of coiled coils from sequence. *Bioinformatics* **22,** 356–358
50. Gilbert, S. P., and Johnson, K. A. (1994) Pre-steady-state kinetics of the microtubule-kinesin ATPase. *Biochemistry* **33,** 1951–1960
51. Hackney, D. D. (1994) Evidence for alternating head catalysis by kinesin during microtubule-stimulated ATP hydrolysis. *Proc. Natl. Acad. Sci. U.S.A.* **91,** 6865–6869
52. Ma, Y. Z., and Taylor, E. W. (1995) Mechanism of microtubule kinesin ATPase. *Biochemistry* **34,** 13242–13251
53. Ma, Y. Z., and Taylor, E. W. (1997) Interacting head mechanism of microtubule-kinesin ATPase. *J. Biol. Chem.* **272,** 724–730
54. Moyer, M. L., Gilbert, S. P., and Johnson, K. A. (1998) Pathway of ATP hydrolysis by monomeric and dimeric kinesin. *Biochemistry* **37,** 800–813
55. Rosenfeld, S. S., Fordyce, P. M., Jefferson, G. M., King, P. H., and Block, S. M. (2003) Stepping and stretching. How kinesin uses internal strain to walk processively. *J. Biol. Chem.* **278,** 18550–18556
56. Rosenfeld, S. S., Jefferson, G. M., and King, P. H. (2001) ATP reorients the neck linker of kinesin in two sequential steps. *J. Biol. Chem.* **276,** 40167–40174
57. Rosenfeld, S. S., Xing, J., Jefferson, G. M., Cheung, H. C., and King, P. H. (2002) Measuring kinesin's first step. *J. Biol. Chem.* **277,** 36731–36739
58. Clancy, B. E., Behnke-Parks, W. M., Andreasson, J. O., Rosenfeld, S. S., and Block, S. M. (2011) A universal pathway for kinesin stepping. *Nat. Struct. Mol. Biol.* **18,** 1020–1027
59. Krzysiak, T. C., Grabe, M., and Gilbert, S. P. (2008) Getting in sync with dimeric Eg5. Initiation and regulation of the processive run. *J. Biol. Chem.* **283,** 2078–2087
60. Krzysiak, T. C., Wendt, T., Sproul, L. R., Tittmann, P., Gross, H., Gilbert, S. P., and Hoenger, A. (2006) A structural model for monastrol inhibition of dimeric kinesin Eg5. *EMBO J.* **25,** 2263–2273
61. Goulet, A., Major, J., Jun, Y., Gross, S. P., Rosenfeld, S. S., and Moores, C. A. (2014) Comprehensive structural model of the mechanochemical cycle of a mitotic motor highlights molecular adaptations in the kinesin family. *Proc. Natl. Acad. Sci. U.S.A.* **111,** 1837–1842
62. Behnke-Parks, W. M., Vendome, J., Honig, B., Maliga, Z., Moores, C., and Rosenfeld, S. S. (2011) Loop L5 acts as a conformational latch in the mitotic kinesin Eg5. *J. Biol. Chem.* **286,** 5242–5253
63. Rosenfeld, S. S., Xing, J., Jefferson, G. M., and King, P. H. (2005) Docking and rolling, a model of how the mitotic motor Eg5 works. *J. Biol. Chem.* **280,** 35684–35695
64. Rosenfeld, S. S., van Duffelen, M., Behnke-Parks, W. M., Beadle, C., Corrreia, J., and Xing, J. (2009) The ATPase cycle of the mitotic motor CENP-E. *J. Biol. Chem.* **284,** 32858–32868